

Label-free phase change detection of lipid bilayers using nanoscale diamond magnetometry

*Hitoshi Ishiwata^{*1,2}, Hiroshi C. Watanabe^{1,3}, Shinya Hanashima⁴,*

Takayuki Iwasaki² and Mutsuko Hatano²

¹PRESTO, Japan Science and Technology Agency, 7 Gobancho, Chiyoda, 152-0076 Tokyo, Japan

²School of Engineering, Department of Electrical and Electronic Engineering, Tokyo Institute of Technology, 2-12-1 Ookayama, Meguro, Tokyo 152-8552, Japan

³Quantum Computing Center, Keio University, 3-14-1 Hiyoshi, Kohoku-ku, Yokohama 223-8522, Japan

⁴Department of Chemistry, Graduate School of Science, Osaka University, 1-1 Machikaneyama, Toyonaka, Osaka 560-0043, Japan

KEYWORDS: Nitrogen-vacancy center, nanoscale magnetometry, lipid bilayer

ABSTRACT:

The NV center in a diamond is a quantum sensor with exceptional quality for highly sensitive nanoscale analysis of NMR spectra and thermometry. In this study, we investigate nanoscale phase change detection of lipid bilayers utilizing ensemble-averaged nuclear spin detection from small volume $\sim (6 \text{ nm})^3$, which was determined by the depth of the NV center. Analysis of nanoscale NMR signal confirm thickness of lipid bilayer to be $6.2 \text{ nm} \pm 3.4 \text{ nm}$ with proton density of 65 proton/nm^3 verifying formation of lipid

bilayer on top of diamond sample. Correlation spectroscopy from nanoscale volume reveals quantum oscillation at 3.06 MHz corresponding to the Larmor frequency of proton at an applied magnetic field of 71.8 mT. The result of the correlation spectroscopy was compared with the 2D molecular diffusion model constructed by Monte Carlo simulation combined with results from molecular dynamics simulation. There is a change in diffusion constant from $1.5 \text{ nm}^2/\mu\text{s}$ to $3.5 \text{ nm}^2/\mu\text{s}$ when the temperature changes from 26.5°C to 36.0°C . Our results demonstrate that simultaneous observation of changes in translational diffusion and temperature is possible in label-free measurements using nanoscale diamond magnetometry. Our method paves the way for label-free imaging of cell membranes for understanding its phase composition and dynamics.

INTRODUCTION:

The cell membrane is a nanoscale 2D fluid crystalline assembly with sub-compartment domains that are critical for cellular functions, including transport of molecules, communications, and metabolic properties with its external medium [1,2,3]. These domains are distinguished by different phases of lipid membranes, and extensive research has focused on understanding the structure and dynamic properties of such domains [4]. The fluidity of the lipid bilayer, described by the 2D translational diffusion of lipid molecules [5], determines the most fundamental property of lipids in different phases and therefore domains. Florescence microscopy has been most effective for measuring fluidity [6, 7]. Most advanced example includes Stimulated Emission Depletion-Fluorescence Correlation Spectroscopy (STED-FCS) utilized for detection of nanoscale diffusion and identification of nanoscale domain [8]. However, the use of fluorescent probes in such a technique changes the mass and structure of target molecules and deteriorates the observed dynamics [9, 10]. For direct measurement of the diffusion constant without additional perturbation in a biological environment, a label-free technique with nanoscale detection volume is necessary. Nanoscale NMR and correlation spectroscopy using a NV center has emerged as a

quantum measurement platform that allows for label-free diffusion measurement with nuclear spin from a small detection volume of $\sim (6 \text{ nm})^3$ [11]. The detection volume is determined by the location of the NV center from the surface of the diamond [12, 13].

The NV Center also allows the detection of local temperature with sub-degree precision [14,15], enabling the simultaneous detection of temperature and diffusion in nanoscale samples in a biological environment, which is optimal for the phase change detection of biological samples. Our measurement technique is compatible with cell membrane measurement and can be achieved by simply placing cells on top of diamond. This measurement technique makes it possible to achieve imaging down to a diffraction-limited spot.

In this study, the NV center was formed as a perfectly aligned Delta doped layer [16] within 10 nm from the surface as a highly sensitive detection probe for the ensemble-averaged detection of nanoscale diffusion in the lipid bilayer. Correlation spectroscopy observed from the NV center revealed a change in relaxation time as a function of change in temperature. Monte Carlo 2D translational diffusion simulation was combined with molecular dynamics simulation to depict dynamics that are observed in our data. Our simulation demonstrated that the translational diffusion constant changed from $1.5 \text{ nm}^2/\mu\text{sec}$ to $3.5 \text{ nm}^2/\mu\text{sec}$ by changing the temperature from $26.5 \text{ }^\circ\text{C}$ to $36.0 \text{ }^\circ\text{C}$. Our simulation demonstrates the phase change from an ordered phase to a rippled or disordered phase.

We report the first direct observation of phase change in the lipid bilayer; this was achieved using the nanoscale detection volume of the NV center. Direct observation of changes in the diffusion constant paves the way for the label-free identification of domains that are formed in the cell membrane to understand the relationship between cell membrane dynamics and cell function [17].

EXPERIMENTAL METHODS:

Figure 1 (a) presents the overall setup of our experiment. A perfectly aligned shallow ensemble NV center was formed 10 nm from the surface through CVD growth [16]. NV center measurements were performed using a home-built optical microscope based on Olympus IX73 for confocal and wide-field measurements [Supporting Information]. Supported lipid bilayer (SLB) was formed using dipalmitoylphosphatidylcholine (DPPC) molecules on top of the shallow NV center using the vesicle fusion method [18]. DPPC was used as the model in this study for the closeness of properties to sphingomyelin (SM), a major constituent of membrane rafts [19]. As shown in Figure 1 (b), DPPC exhibits an ordered phase at $\sim 25^\circ\text{C}$ and as the temperature is raised to close to T_m (transition temperature) of DPPC $\sim 41^\circ\text{C}$, a phase change occurs in the DPPC toward the disordered phase [20]. Phase change introduces changes in translational diffusion rates in the lipid bilayer. To measure the change in diffusion rates of the lipid bilayer, an optically defined averaged readout from a shallow ensemble NV center with a detection volume $\sim (6\text{ nm})^3$ was used for nanoscale NMR and correlation spectroscopy [Supporting Information]. Application of correlation spectroscopy using pulse sequence shown in Figure 1 (a), allows comparison of the detected phase accumulated in the NV center between two XY8-N measurements spaced by τ . Correlation spectroscopy has been shown to detect 3D nanoscale diffusion of protons in oil [11]. In this study, we applied this technique to high density ($\sim 60\text{ nm}^{-3}$) proton nuclear spins in a lipid bilayer to study the diffusion characteristics, as shown in Figure 1 (b).

The sample was placed in an incubator as shown in Figure 1 (a) to control temperature and maintain a steady temperature. For precise interpretation of phase transition, high-precision measurement of temperature is extremely important. Detection of the difference between bright $|0\rangle$ and dark $|1\rangle$ states enables readout of the resonance frequency $D(T)$ that depends on the local temperature T . The temperature dependence is $dD(T)/dT = -74\text{ kHz/K}$ [21]. We applied the pulse sequence shown in Figure 1 (a) known

as Thermal Echo (T-Echo) [22, 23] to determine $D(T)$ of the NV center by changing the applied frequency and measuring the observed oscillation frequency.

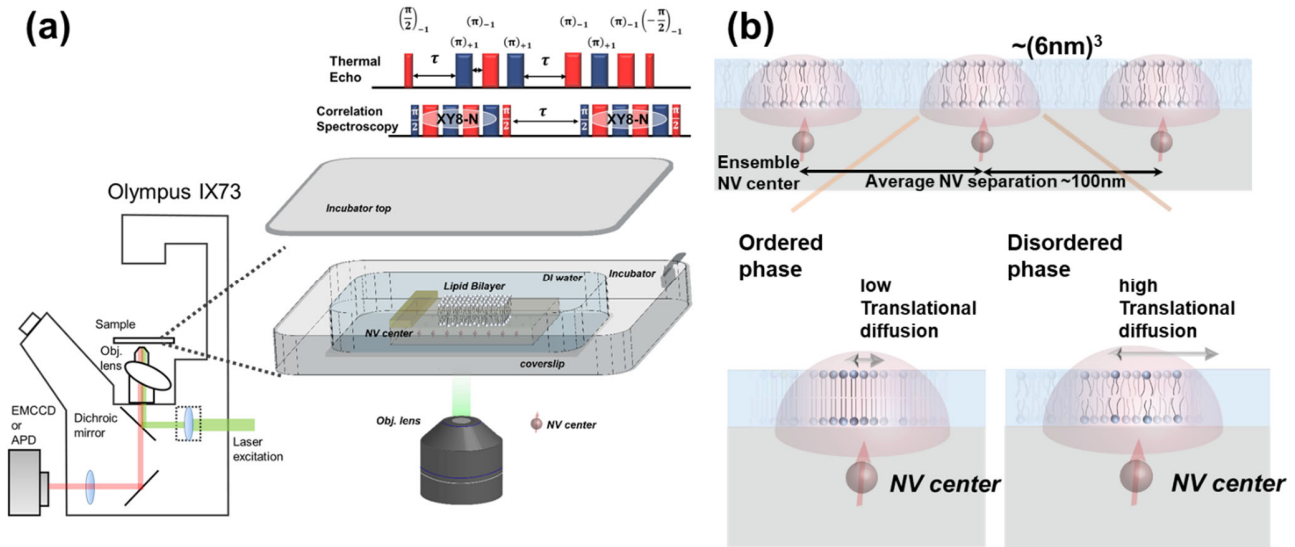


Figure 1. (a) Schematic for NV measurement system and used pulse sequences. (b) Schematic for phase change detection of lipid bilayer using shallow ensemble NV center.

Lissamine Rhodamine B 1,2-Dihexadecanoyl-sn-Glycero-3-Phosphoethanolamine (Rhodamine-PE, Thermo Fisher Scientific) was mixed at 1 % mol with 1,2-dipalmitoyl-sn-glycero-3-phosphocholine (DPPC, Avanti Polar Lipids) in PBS buffer. DPPC was dissolved in PBS at 0.5 mg/mL concentration and sonicated in a warm water bath at 60 °C for 5–15 min. After sonication, the sample was incubated for at least 1 h on a hot plate at 70 °C. After incubation, the sample was sonicated in a warm water bath at 60 °C until a transparent sample was obtained. CVD-grown diamond samples with a shallow NV center were exposed to an acid treatment with a 1 : 3 mixture of HNO_3 and H_2SO_4 at a hotplate temperature of 400 °C for 45 min, followed by rinsing with deionized water to obtain an oxygen-terminated surface. XPS measurements of the acid-treated diamond samples confirmed increased oxygen coverage for confirmation of the oxygen termination of the surface. 100 μL of DPPC/Rhodamine-PE solution was

deposited on top of diamond sample and incubated for 20 min. After incubation, 1 mL of PBS solution was injected onto diamond, and sample wash was performed ten times.

The sample was excited with a 532 nm laser with a dichroic mirror (LPF at 600 nm) using a 40x objective lens (Olympus LCACHN40XIPC) and detected with a color camera (V230CFL or DP53). Figure 2 (a) depicts a typical image of a diamond sample with excitation with a 532 nm laser. Emission above 600 nm from Rhodamine B was confirmed on top of the diamond. The formation of the lipid bilayer was confirmed through florescent recovery after photobleaching (FRAP). Laser excitation was applied at a high intensity of $\sim 10^5$ mW/cm² for more than 5 min to perform photobleaching, where emission from Rhodamine B was depleted. Figure 2 (b) presents a typical image obtained after bleaching of the sample. Depletion of emission was confirmed on the spot defined by Iris used to block the laser. As shown in Figure (c), the DPPC/Rhodamine-PE sample showed recovery of emission after 5 min. FRAP measurement proved the existence of a lipid bilayer on top of the diamond sample.

Nanoscale NMR measurements were performed using a confocal setup for protons in the DPPC sample without rhodamine B to confirm the existence of DPPC on top of the shallow NV center. Sample preparation was applied in the same manner as DPPC/Rhodamine-PE described above, except that Rhodamine-PE was not introduced, and only DPPC (1,2-Dipalmitoyl-3-PC, 13C32, Larodan) was used as the molecule for deposition. DI water was used instead of PBS solution. For nanoscale NMR measurements, a magnetic field of 71.8 mT was applied and confirmed from the ODMR spectrum of the NV center. The proton signal was observed by application of the XY8-40 sequence. A schematic representation of the estimation of lipid bilayer thickness t_{LB} is presented in Figure 2 (d). The proton density and proton thickness of the lipid bilayer were calculated using the equation below [12].

$$C(\tau) \approx \exp\left[-\frac{2}{\pi^2} \gamma_e^2 B_{RMS}^2 K(N\tau)\right], B_{RMS}^2_{calib.} = \rho \left(\frac{\mu_0 \hbar \gamma_n}{4\pi}\right)^2 \left(\frac{\pi}{16d_{NV}^3}\right) [1]$$

$$B_{RMS\ lipid\ bilayer}^2 = \rho \left(\frac{\mu_0 \hbar \gamma_n}{4\pi} \right)^2 \left(\frac{\pi}{16} \right) \left[\frac{1}{(d_{NV} + z_{LB\ bottom})^3} - \frac{1}{(d_{NV} + z_{LB\ top})^3} \right] [2]$$

Initially, the depth of the NV center was calibrated by measuring the protons in oil and using Eq.1 to evaluate the depth of the NV center to be 6.6 ± 0.5 nm. Using the calibrated value, the thickness of the lipid bilayer and the density of protons in the lipid bilayer were calculated using Eq.2. The calculated thickness of the lipid bilayer was estimated to be 6.2 ± 3.4 nm with a proton density of 65 [proton/nm³]. The lipid packing density estimated from proton density ~ 0.49 [nm²/lipid] is comparable to the reported lipid packing density 0.47 [nm²/lipid] for DPPC [24]. Our measurement confirms the formation of DPPC molecules on top of the diamond sample.

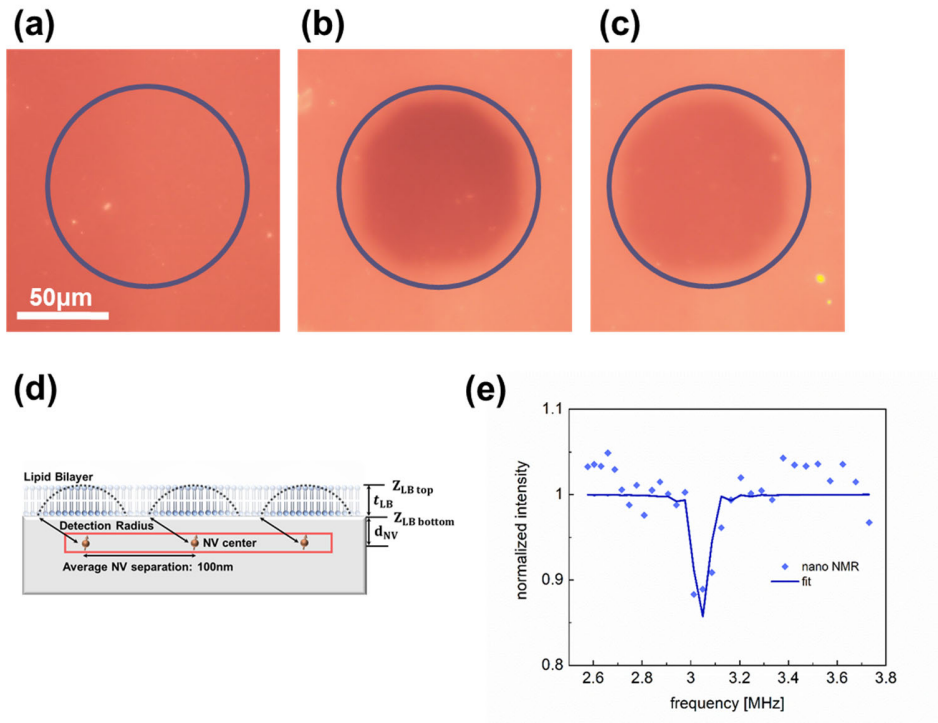


Figure 2. Emission observed for DPPC/Rhodamine-PE (a) after deposition (b) after photo bleaching (c) 5min. after photo bleaching. (d) Schematic representation for definition used to calculate thickness and density of Lipid Bilayer (e) Nanoscale NMR measurement performed on DPPC with applied magnetic field of 71.8 mT.

THEORETICAL CALCULATIONS AND RESULTS:

Calculation of diffusion constant from correlation spectroscopy requires detailed modeling of dynamics for observed nuclear spin. A previous study demonstrated a 3D diffusion model for proton nuclear spin in oil [11]. The relaxation rate observed in correlation spectroscopy is determined by two factors, T_2 of observed nuclear spin and probability of detecting nuclear spin within the detection volume determined by the depth of the NV center. Because we observe proton spins with the $S=1/2$ system, the contribution to T_2 is determined by dipolar coupling between protons [25, 26]. As shown in Figure 3(a), the molecular dynamics of the lipid bilayer were divided into intramolecular and intermolecular parts, where the intramolecular part was used to model the rotation and wobble effect, and the intermolecular part was used to model the effect of diffusion. Equations used for calculation of T_2 are given below [26]: where r is the intramolecular distance between two protons in the lipid molecule, γ_H is the proton gyromagnetic ratio, ω_H is the proton Larmor frequency, \hbar is the Dirac constant, $\tau_{c\text{rot.}}$ is the correlation time for rotation, N is the density of proton in the lipid bilayer, d is the intermolecular distance between two protons, and $\tau_{c\text{trans.}}$ is the correlation time for translation.

$$\frac{1}{T_{2\text{ intra.}}} = \frac{3}{20} \frac{\gamma_H^4 \hbar^2}{r^6} \left[3\tau_{c\text{rot.}} + \frac{5\tau_{c\text{rot.}}}{1 + \omega_H^2 \tau_{c\text{rot.}}^2} + \frac{2\tau_{c\text{rot.}}}{1 + 4\omega_H^2 \tau_{c\text{rot.}}^2} \right] \quad [3]$$

$$\frac{1}{T_{2\text{ inter.}}} = \frac{2\pi}{10} \frac{N\gamma_H^4 \hbar^2}{d^3} \left[3\tau_{c\text{trans.}} + \frac{5\tau_{c\text{trans.}}}{1 + \omega_H^2 \tau_{c\text{trans.}}^2} + \frac{2\tau_{c\text{trans.}}}{1 + 4\omega_H^2 \tau_{c\text{trans.}}^2} \right] \quad [4]$$

As shown in Figure 3(b), molecular dynamics (MD) simulation was used for dynamics in a small time scale of ~ 50 ns to calculate r , d , N , and $\tau_{c\text{rot.}}$. r , d , and N were all estimated from the integrated radially distributed function (RDF) (SI Fig.S2 (b),(c)). $\tau_{c\text{rot.}}$ was determined by estimating the correlation time for vector defined along the acid chain of DPPC (SI Fig.S2(d)). The results from MD simulation were combined with Monte Carlo simulation to calculate the change in the probability of detection in nanoscale

magnetometry with a diffusion constant as the only free parameter for fitting to our model. The change in the probability of detection was calculated using a 2D diffusion model, where the overlap between the diffusion area and detection area was calculated to extract the change in the probability of diffusion (SI Fig.S3(c) and (d)). The detection area was calculated in detail using a model from a previous report [13] (SI Fig.S1(a) and (b)).

To measure the phase transition in DPPC molecules, the temperature setting in the incubation chamber was used to change the temperature, and the NV center was used as a local probe for quantum thermometry using the Thermal-Echo (T-Echo) method. Pulse sequence was applied in a confocal setup at dual frequency to remove the effect of the magnetic field during measurement for precise measurement of $D(T)$ values below 1 °C precision. The results are shown in Figure 3 (c) and (d), where the energy difference between the bright $|0\rangle$ and dark $|1\rangle$ states were observed as oscillations in the T-Echo signal. The T-echo signal without heat supply from the incubator resulted in a $D(T)$ value of $+0.10 \text{ MHz} \pm 24 \text{ kHz}$. The temperature at this measurement setting was calibrated with a K class thermocouple (TM 300) to be 26.5 °C. T-Echo measurement with a temperature setting of 45 °C in an incubator resulted in a $D(T)$ value of $-0.59 \text{ MHz} \pm 44 \text{ kHz}$. The difference in the value of $D(T)$ between the two temperature settings provides a temperature difference of 9.45 °C with a 0.47 °C temperature precision determined by the distribution of the value for different frequencies of the applied pulse on T-Echo. All measurements at different temperature were carried after at least 12 hours of waiting time to stabilize temperature.

For both 26.5 °C and 36.0 °C, correlation spectroscopy was performed using an EMCCD camera as the detector for diffusion analysis of protons in DPPC molecules. The ODMR spectrum obtained from the NV center was used to determine the applied magnetic field of 71.8 mT. Figure 3 (e) and (f) show correlation spectrum obtained for 1.6 μsec to 20 μsec . Oscillation at 3.06 MHz is confirmed at both temperatures from analysis of the obtained spectrum performed for shorter time with higher resolution.

And signal was not observed for same measurement time in the case of sample without lipid bilayer on top. The obtained data are compared with Monte Carlo simulation results in Figure 3 (e) and (f). As shown in Figure 3 (e), the correlation spectrum obtained at 26.5 °C shows relaxation characteristic comparable to the simulation with a diffusion constant Dt of 1.5 nm²/μsec. As the temperature is increased to 36.0 °C, the relaxation characteristic shows result similar to the simulation with a diffusion constant of 3.5 nm²/μsec, as shown in Figure 3 (f). Both measurements were performed on same location, calibrated at diffraction limited resolution (~300nm) by confocal scan of step-edge structure [16] observed on shallow ensemble NV centers. These measurements confirmed observation of phase change through change in the diffusion constant of DPPC molecules.

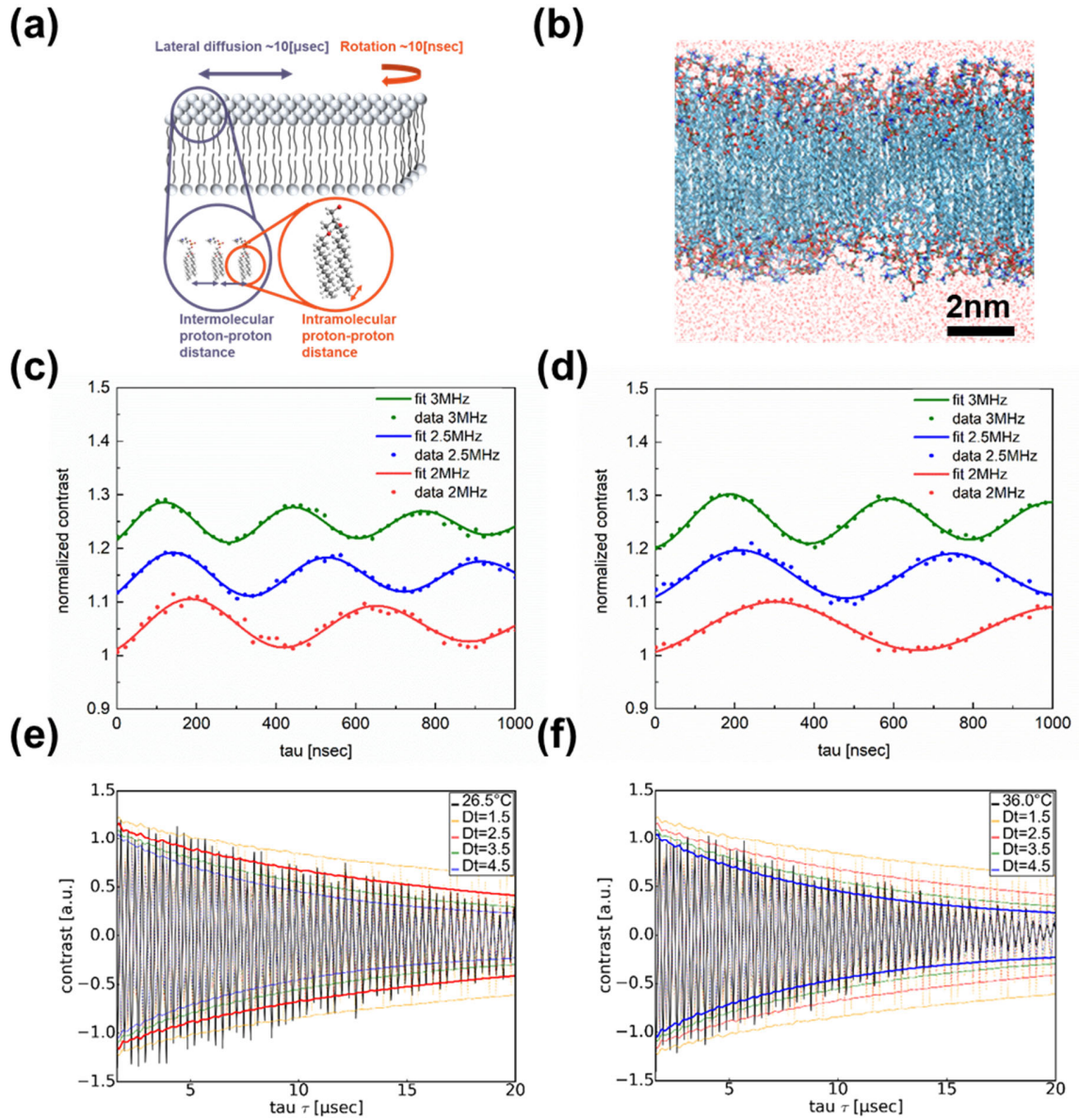


Figure 3. (a) Schematic for modeling of lipid bilayer. Lateral diffusion and rotation were separated for different time scales. Dipolar interaction was conceived for each dynamic by considering intermolecular and intramolecular proton-proton distance. (b) Molecular dynamics simulation on DPPC at 25 °C. Simulation was performed for 50 ns with 1 psec resolution. (c) T-Echo measurement performed at 26.5 °C for different set frequency relative to $D(T)$ value. (d) T-Echo measurement performed at 36.0 °C for different set frequency relative to $D(T)$ value. Correlation spectroscopy performed at (e) 26.5 °C and (f) 36.0 °C.

DISCUSSION AND CONCLUSIONS:

Figure 4 presents the diffusion constants obtained from different techniques on DPPC molecules [27, 28, 29, 30]. Techniques that involve a fluorescent marker, such as FRAP and Marker Quench, exhibit diffusion constants that have an order of magnitude significantly lower than that of label free techniques, such as magic angle spinning pulse field gradient NMR (MAS PFG NMR). This could be a drawback of fluorescent markers with heavy mass or structural changes influenced by the marker [31, 32]. In addition, results from FRAP have been reported to vary significantly because of the selected marker [32], and this is demonstrated by comparing two experiments performed on SLB of DPPC, as shown in Figure 4. The diffusion constant obtained from K. Lukas et al. with the NBD-PE marker differed significantly from the results of C. Scomparin et al. with the 16:0-12:0 NBD PC marker. In addition, K. Lukas et al. observed the existence of a ripple phase between 32 °C and 40 °C, whereas Scomparin et al. failed to identify such a phase. These results demonstrate variation and deterioration in the observation of lipid dynamics using fluorescent marker techniques.

Our results obtained from nanoscale diamond magnetometry are consistent with the results obtained from MAS PFG NMR. MAS PFG NMR allows precise diffusion measurements without special labeling of the investigated molecules, which may alter molecular properties [33]. However, uniformity on structure of lipid membranes are necessary for modeling and radius curvature of membranes have to be larger than 1 μm due to the limitations imposed by the field gradient applied for measurement. Therefore, MAS PFG NMR is not suited for direct measurement of actual cell membranes.

Our measurement technique, using extremely small detection volume defined by the depth of the NV center, allows label-free measurement of diffusion constants that are comparable to reported values from MAS PFG NMR without complication imposed by sample preparation and measurement system. Our finding lay the foundations for the label-free identification of domains that are formed in the cell

membrane to understand the relationship between cell membrane dynamics and cell function. It is also compatible with direct imaging of cell membranes without any label introduction, leading to future biological applications such as cell membrane diagnosis.

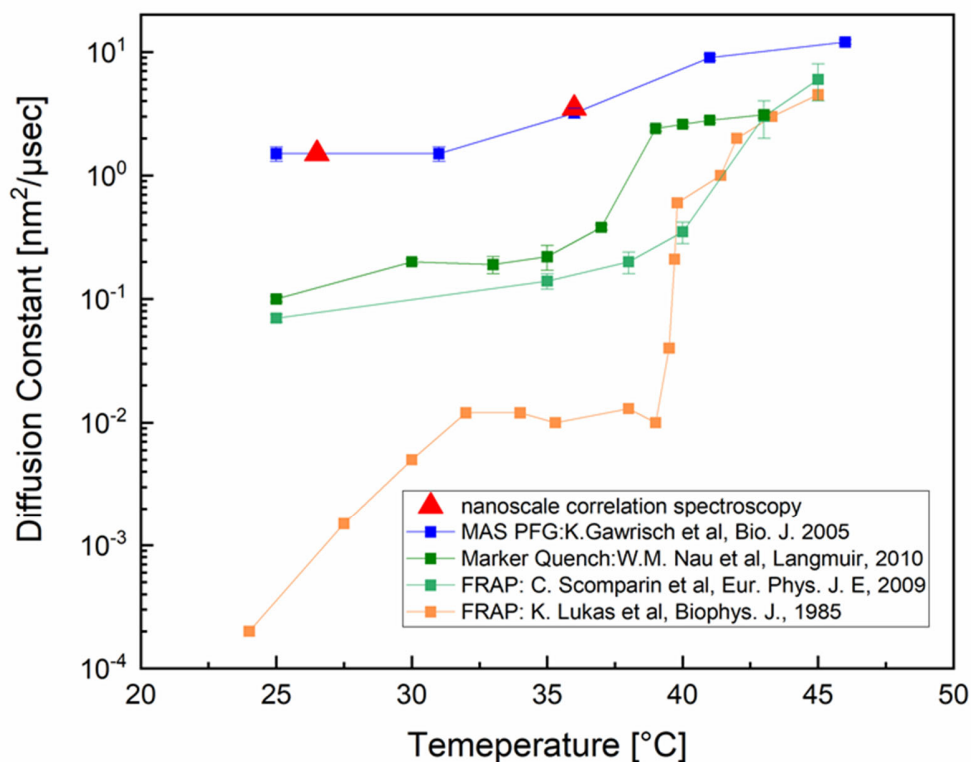


Figure 4. Comparison of diffusion constants obtained for different temperatures with different measurement techniques on DPPC molecules. Error bars were provided as indicated in each manuscript.

ASSOCIATED CONTENT:

Supporting Information.

The Supporting Information is available free of charge.

NV measurement system, NV center sample, MD simulation, Definition of detection volume of NV center, Details of MD simulation, 2D diffusion model (PDF)

AUTHOR INFORMATION

Corresponding Author

*E-mail: ishiwata.h.aa@m.titech.ac.jp

Author Contributions

H.I. conceived the concept, built the experimental setup for nanoscale NMR, correlation spectroscopy, and T-echo, fabricated shallow ensemble NV center, fabricated lipid bilayers, performed the measurements, built Python code for Monte Carlo 2D molecular diffusion analysis, analyzed the data, and wrote the manuscript. H.W. built and performed the MD simulation. S.H. advised lipid bilayer discussion and preparation. H.I., H.W., S.H., T.I., and M.H. discussed the study.

Notes

The authors declare no competing financial interest.

ACKNOWLEDGMENT

This research was supported by JST PRESTO Grant number JPMJPR17G1 and JPMJPR17GC, JSPS Grant Number 20K03885 and 20H05518 and the MEXT Quantum Leap Flagship Program (MEXT Q-LEAP) Grant Number JPMXS0118067285 and JPMXS0118067395.

REFERENCES:

1. K. Simons, W. L. C. Vaz, model systems, lipid rafts, and cell membranes. *Annu Rev Biophys Biomol Struct* 33:269–295 (2004).
2. G. van Meer G, A. I. P. M. de Kroon, Lipid map of mammalian cells. *J Cell Sci* 124:5–8 (2011).
3. J. Lombard, Once upon a time the cell membranes: 175 years of cell boundary research. *Biol Direct* 9:32 (2014).
4. E. Sezgin, I. Levental, S. Mayor, C. Eggeling, The mystery of membrane organization: composition, regulation, and roles of lipid rafts. *Nat. Rev. Mol. Cell Biol.* 18, 361–374 (2017).
5. Van Meer G, Voelker DR, Feigenson GW, Membrane lipids: Where they are and how they behave. *Nat. Rev. Mol. Cell Biol.* 9, 112–124 (2008).
6. S. L. sVeatch, S. L. Keller, Seeing spots: Complex phase behavior in simple membranes. *Biochim. Biophys. Acta.* 1746, 172–185 (2005).
7. Kress A, et al., Mapping the local organization of cell membranes using excitation polarization-resolved confocal fluorescence microscopy. *Biophys. J.* 105, 127–136 (2013).
8. C. Eggeling, et al.. Direct observation of the nanoscale dynamics of membrane lipids in a living cell. *Nature.* 457, 1159–1162 (2009).
9. E. Sezgin, et al.. Partitioning, diffusion, and ligand binding of raft lipid analogs in model and cellular plasma membranes. *Biochim Biophys Acta.* 1818(7), 1777–1784 (2012).
10. M. Skocaj, et al.. The sensing of membrane microdomains based on poreforming toxins. *Curr. Med. Chem.* 20(4), 491–501 (2013).
11. T. Staudacher, N. Raatz, S. Pezzagna, J. Meijer, F. Reinhard, C. A. Meriles, J. Wrachtrup, Probing molecular dynamics at the nanoscale via an individual paramagnetic center. *Nat. Comm.* 6, 8527 (2015).
12. L. M. Pham, S. J. DeVience, F. Casola, I. Lovchinsky, A. O. Sushkov, E. Bersin, J. Lee, E. Urbach, P. Cappellaro, H. Park, A. Yacoby, M. Lukin, R. L. Walsworth, NMR technique for determining the depth of shallow nitrogen-vacancy centers in diamond. *Phys. Rev. B* 93, 045425 (2016).
13. T. Staudacher, F. Shi, S. Pezzagna, J. Meijer, J. Du, C. A. Meriles, F. Reinhard, J. Wrachtrup, nuclear magnetic resonance spectroscopy on a (5-Nanometer)³ sample volume. *Science.* 339, 561 (2013).
14. G. Kucsko, P. C. Maurer, N. Y. Yao, M. Kubo, H. J. Noh, P. K. Lo, H. Park, M. D. Lukin, Nanometre-scale thermometry in a living cell. *Nature.* 500, 54-59 (2013).
15. P. Neumann, I. Jakobi, F. Dolde, C. Burk, R. Reuter, G. Waldherr, J. Honert, T. Wolf, A. Brunner, J. H. Shim, D. Suter, H. Sumiya, J. Isoya, J. Wrachtrup, High-Precision Nanoscale Temperature Sensing Using Single Defects in Diamond. *Nano. Lett.* 13, 2738-2742 (2013).
16. H. Ishiwata, M. Nakajima, K. Tahara, H. Ozawa, T. Iwasaki, M. Hatano, Perfectly aligned shallow ensemble nitrogen-vacancy centers in (111) diamond. *APL.* 111, 043103 (2017).
17. M. A. Pavela, E. N. Petersena, H. Wanga, R. A. Lerner, S. B. Hansen, Studies on the mechanism of general anesthesia. *Proc. Natl. Acad. Sci. USA* 117, 13757-13766 (2020).
18. A. Akesson, T. Lind, N. Ehrlich, D. Stamou, H. Wacklinc, M. Cardenas, Composition and structure of mixed phospholipid supported bilayers formed by POPC and DPPC. *Soft Matter*, 8, 5658 (2012).
19. D. A. Brown, E. London, Structure and Function of sphingolipid - and cholesterol-rich membrane wafers. *J. Biol. Chem.* 275, 17221-17224 (2000).

20. S. Mabrey, J. M. Sturtevant, Investigation of phase transitions of lipids and lipid mixtures by high-sensitivity differential scanning calorimetry. *Proc. Natl. Acad. Sci. USA* 73, 3862-3866 (1976).
21. V. M. Acosta, et al., Temperature dependence of nitrogen-vacancy magnetic resonance in diamond. *Phys. Rev. Lett.* 104(7), 070801 (2010).
22. D. M. Toyli, C. F. de las Casasa, D. J. Christlea, V. V. Dobrovitskii, D. D. Awschalom, Fluorescence thermometry enhanced by the quantum coherence of single spins in diamond. *Proc. Natl. Acad. Sci. USA* 110, 8417-8421 (2013).
23. J. Wang, F. Feng, J. Zhang, J. Chen, Z. Zheng, L. Guo, W. Zhang, X. Song, G. Guo, L. Fan, C. Zou, L. Lou, W. Zhu, G. Wang, High-sensitivity temperature sensing using an implanted single nitrogen-vacancy center array in diamond. *Phys. Rev. B* 91, 155404 (2015).
24. S. Tristram-Nagle, R. Zhang, R. M. Suter, C. R. Worthington, W. J. Sun, J. F. Nagle, Measurement of chain tilt angle in fully hydrated bilayers of gel phase lecithins. *Biophys. J.* 64, 1097-1109 (1993).
25. M. H. Levitt, *Spin Dynamics*. 2nd ed. software (Wiley, 2015).
26. A. G. Lee, N. J. M. Birdsall, J. C. Metcalfe, Ch. 1 Nuclear magnetic relaxation and the biological membrane. *Methods in membrane biology*. (Plenum Press, 1974)
27. C. Scomparin, S. Lecuyer, M. Ferreira, T. Charitat, B. Tinland, Diffusion in supported lipid bilayers: Influence of substrate and preparation technique on the internal dynamics. *Eur. Phys. J. E.* 28, 211-220 (2009).
28. L. K. Tamm, H. M. McConnell, Supported phospholipid bilayers. *Biophys. J.* 47, 105-113 (1985).
29. R. Meyer, A.F.-P. Sonnen, W.M. Nau, Phase-dependent lateral diffusion of α -tocopherol in DPPC liposomes monitored by fluorescence quenching. *Langmuir*. 26(18), 14723-14729 (2010).
30. H. A. Scheidt, D. Huster, K. Gawrisch, Diffusion of Cholesterol and Its Precursors in Lipid Membranes Studied by ^1H Pulsed Field Gradient Magic Angle Spinning NMR. *Biophys. J.* 89, 2504-2512 (2005).
31. M. L. Wagner, L. K. Tamm, Tethered polymer-supported planar lipid bilayers for reconstitution of integral membrane proteins: silane-polyethyleneglycol-lipid as a cushion and covalent linker. *Biophys. J.* 79(3), 1400-1414 (2000).
32. L. K. Tamm, Lateral diffusion and fluorescence microscopy studies on a monoclonal antibody specifically bound to supported phospholipid bilayers. *Biochemistry*. 27(5), 1450-1457 (1988).
33. H. A. Scheidt, P. Muller, A. Herrmann, D. Huster, The potential of fluorescent and spin-labeled steroid analogs to mimic natural cholesterol. *J. Biol. Chem.* 278, 45563-45569 (2003).

Supplementary Information

NV measurement system:

The breadboard was placed inside Olympus IX-73 to guide the laser into the objective lens through a dichroic mirror. The detector side could be switched to an EM-CCD camera (iXonUltra) or a pinhole with an APD detector (SPCM-AQRH-14-FC-ND) or a color CCD camera (V230CFL or DP53) through the adjuster placed on the lower deck of IX-73. The incubator was placed inside the piezo stage (P-545.3C8S) to control the temperature with a thermocoupled-heater in order to change the temperature of our system. MW was delivered to the NV center through a 20 μm diameter copper wire with a sputtered Ti/Cu/Au electrode on a cover slide. Microwaves were delivered from the SG (Anritsu MG3700A and SynthHD PRO Dual RF Signal Generator) combined with an amplifier (R&K CGA701M62-444R or Amplifier Research Model 50W1000A). The pulse sequence was controlled by DTG5274 and the MW pulse was truncated by a switch (Mini circuit ZASWA-2-50DRA+). A high-power laser (Verdi G5) was pulsed through an AOM(Gooch Housego Model:3250-220) with an RF driver (3910-XX).

NV center sample (definition of ensemble average readout):

A perfectly aligned shallow NV ensemble was formed within 10 nm from the surface by the CVD growth technique with step flow growth. (ref. 16)

In the case of shallow ensemble NV center, performing nanoscale NMR or correlation spectroscopy results in each individual single NV center detecting detection volume at depth defined by depth of NV center. In the optical readout process, each phase detected at individually independent (ensemble) NV centers are readout as averaged from optically defined detection area. In this paper, optically defined area was $\sim 300\text{nm}$ diameter defined by optical diffraction-limited.

Definition of detection volume of NV center:

The detection volume for the shallow ensemble NV center was calculated following Monte Carlo simulation used to calculate the detection volume used in previous work (ref. 13). The density of proton in the lipid bilayer was estimated from molecular dynamics simulation and results obtained from nanoscale NMR measurements using NV center. Monte Carlo simulation was performed under the assumption of ~5nm thickness lipid bilayer and therefore no detectable proton above ~5nm from the surface. (proton in DI water is ignored because of its extremely high diffusion coefficient). The following equations were used to calculate the detection volume for the case of nanoscale proton detection in the lipid bilayer, as shown in Figure S1 (a) and (b). The detection volume is defined as the volume of proton contributing to 70% of the total signal detected at the depth of the NV center.

$$B_{rms,i} = \sqrt{\frac{2}{3} \left(\frac{3\mu_0\mu_p}{4\pi r_i^3} \right) \left(\frac{5\pi}{96} \right) \sqrt{(\vec{e}_2 \cdot \vec{n}_l)(\vec{e}_1 \cdot \vec{n}_l))^2 + (\vec{e}_3 \cdot \vec{n}_l)(\vec{e}_1 \cdot \vec{n}_l))^2}} \quad [S1]$$

$$B(N) = \sqrt{\sum_{i=0}^N B_{rms,i}^2} \quad [S2]$$

The number of protons contributing to 70% of the total signal was estimated as shown in Figure 1 (b), and the calculated number of protons was converted to the detection volume and detection area by assuming a thickness of ~ 5 nm for the lipid bilayer. The detection area was found to be 6nm in radius from these calculations.

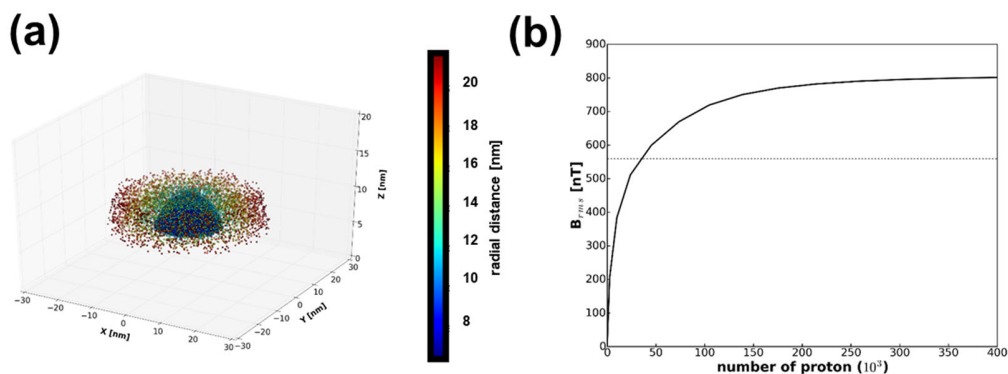


Figure S1(a) 3D mapping of radial distribution of detected nuclear spin from Lipid Bilayer. Different color represents difference in radial distance from NV center. (b) Monte Carlo simulation results of detected B_{rms} signal as function of total detected number of protons. Dotted line shows 70% line from saturation value of B_{rms} .

Details of MD simulation

The MD simulations were conducted using the Fujitsu PRIMEGY CX600M1/CX1640M1 (Oakforest-PACS) and SGI Rackable C1102-GP8 (Reedbush). The lipid bilayer systems were constructed using CHARMM-GUI [S1], where the bilayers consist of 200 lipids in a periodic cubic box with a side length of 10 nm perpendicular to the membrane (Figure S2 (a)). As the forcefield parameters, the CHARMM36 [S2] and TIP3P [S3] models were employed for lipid and water molecules, respectively. After energy minimization, the systems were equilibrated for 4.0 ns by applying a Berendsen Barostat [S4] of 1.0 bar and Berendsen thermostat at target temperatures, 298 K, 310 K, and 314 K, respectively. The MD production runs were carried out under canonical conditions using a Nosé – Hoover thermostat [S5] of respective target temperatures with a time constant of 0.5 ps. The electrostatic interactions were evaluated using the particle-mesh Ewald method with a switching function for electrostatic interactions. The electrostatic interactions in real space and Van der Waals interactions were damped to zero with a switching function in the range of 8.5 and 9.0 Å. The intra/intermolecular radial distribution functions were evaluated for all hydrogen atoms in the fatty acid chain, where the hydrogen atoms in the head group and water were excluded.

Integrated RDF was used to calculate the intramolecular and intermolecular closest average proton–proton distances. Typical results for integrated RDF is shown in Figure S2 (b), where the closest proton-to-proton distance was estimated to be 1.88 Å. This value is comparable to the proton distance between two protons bonded to the same carbon on the acidic chain. To calculate the intramolecular closest average proton to proton distance, protons on the acidic chain of a single molecule were used. This is demonstrated in integrated radial distribution functions for a long radius. As demonstrated in Figure S2 (c), when the radius from a single proton approaches a 3 nm, number of protons saturates to a value equal to that of an acid chain part of single DPPC molecule. A similar calculation technique was used to calculate the intermolecular closest average proton to proton distance. In this case, proton from the same DPPC molecule was eliminated in the calculation, and only the contribution from other DPPC molecules was calculated in the RDF.

For rotational analysis, we selected four carbon atoms C21, C216, C31, and C316, where C21 and C31 were neighboring to the headgroup while C216 and C316 were located at the tails of the fatty acid chains. Then, the second rank auto-correlation functions of rotations of two vectors C21-C216 and C31-C316 of DPPC are evaluated using trajectories of 400 ns at 298.15 K and 314.15 K, respectively. The obtained auto-correlation functions were well fitted by a linear combination of three exponential curves, which resulted in larger correlation coefficients than 0.98. All simulations were conducted using the GROMACS version 2018-3. [S6]

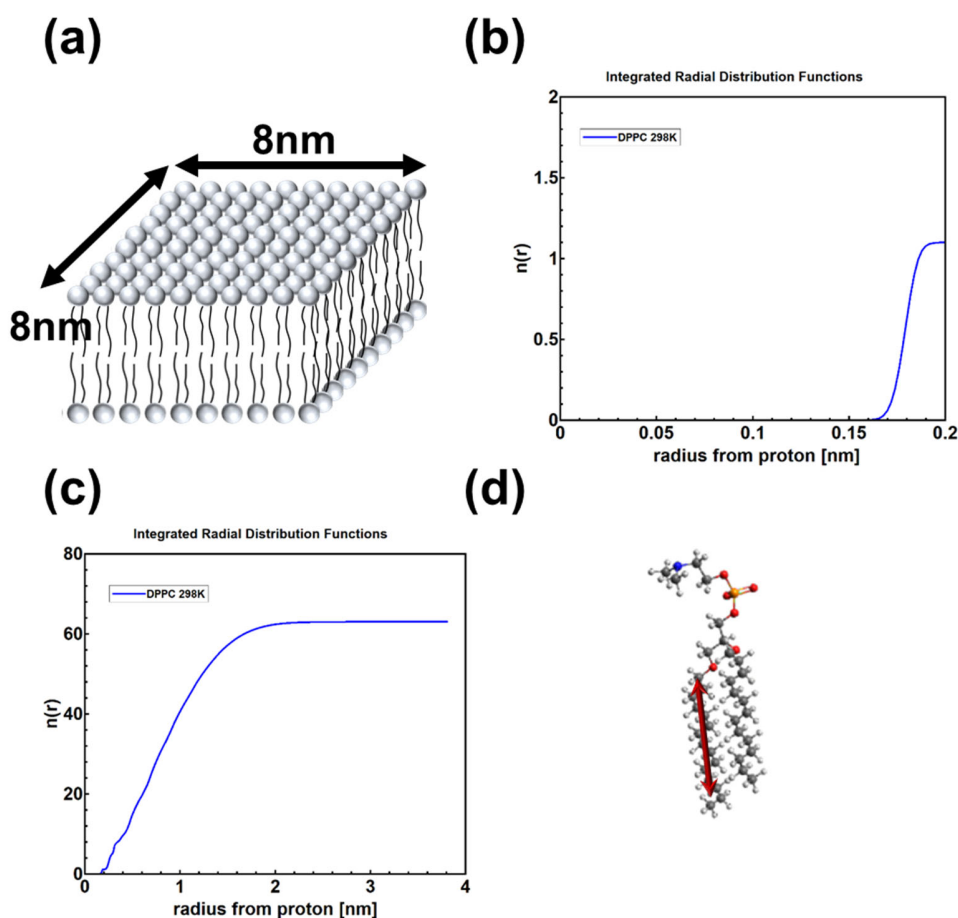


Figure S2: (a) Schematic representation for lipid model used for DPPC MD simulation. 10 lipid x 10 lipid configuration with double layer configuration was used for simulation with total of 200 molecules. (b) RDF calculation for intramolecular closest proton average distance. Calculated by integrated radial distribution functions. Showing 1.88 Å for closest proton. (c) Integrated RDF for larger radius from proton. Showing total number of protons for each lipid. (d) Model used for calculation of rotation of DPPC molecules. Vector connecting first carbon on acidic chain and last carbon (16th carbon) on acidic chain is used to analyze rotation and wobble of DPPC molecules.

2D diffusion model:

Figure S3 (a) shows a schematic representation of the modeling of 2D diffusion dynamics in the lipid bilayer. As shown in Figure S3 (b), a random starting position was selected within the detection area, and the diffusion area was calculated using eq. S3 to calculate diffusion radius for the change in diffusion time. D_{lb} is diffusion constant of lipid bilayer and t_{diff} is diffusion time. The cross section between the diffusion area and detection area was calculated and divided by the

diffusion area to calculate the probability of detection at the corresponding diffusion time. For example, the case shown in Figure S3 (c) represents the case where the detection probability is given as 1 because of the complete overlap between the diffusion area and detection area. Figure S3 (d) shows the case where the probability of detection is given by the overlap between the diffusion area and detection area divided by the diffusion area. The overlap between the diffusion area and detection area was calculated using eq. S4. d is distance between center of detection area and diffusion area and r_{DV} is the radius of detection area. These two cases were applied for all randomly selected starting points, and random points were picked for the number of nuclear spins inside the detection volume.

$$r_{diff} = \sqrt{4D_{lb}t_{diff}} \quad [S3]$$

$$A(d, r_{diff}, r_{DV}) = r_{diff}^2 \cos^{-1} \left(\frac{d^2 + r_{diff}^2 - r_{DV}^2}{2dr_{diff}} \right) + r_{DV}^2 \cos^{-1} \left(\frac{d^2 + r_{DV}^2 - r_{diff}^2}{2dr_{DV}} \right) - \frac{1}{2} \sqrt{(-d + r_{diff} + r_{DV})(d + r_{diff} - r_{DV})(d - r_{diff} + r_{DV})(d + r_{diff} + r_{DV})} \quad [S4]$$

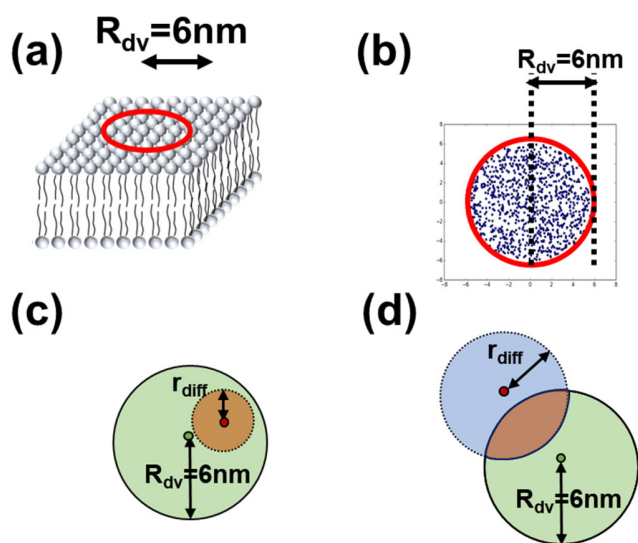


Figure S3: (a) Schematic representation for definition of diffusion area (b) Distribution example of randomly distributed initial point for calculation of diffusion area. (c) Example of calculation of diffusion area and detection area. In the case represented in this figure diffusion area is completely included in detection area. In this case probability of detection is calculated as 1. (d) Example of calculation for cross section of diffusion area and detection area. In this case, overlap between diffusion area and detection area will be divided by area of diffusion area to calculate probability for detection of nuclear spin.

References:

- S1 Jo, S.; Kim, T.; Iyer, V. G.; Im, W. CHARMM-GUI: A Web-Based Graphical User Interface for CHARMM. *J. Comput. Chem.* **2008**, *29* (11), 1859–1865.
- S2 Klauda, J. B.; Venable, R. M.; Freites, J. A.; O'Connor, J. W.; Tobias, D. J.; Mondragon-Ramirez, C.; Vorobyov, I.; MacKerell, A. D.; Pastor, R. W. Update of the CHARMM All-Atom Additive Force Field for Lipids: Validation on Six Lipid Types. *J. Phys. Chem. B* **2010**, *114* (23), 7830–7843.
- S3 Jorgensen, W. L.; Chandrasekhar, J.; Madura, J. D.; Impey, R. W.; Klein, M. L. Comparison of Simple Potential Functions for Simulating Liquid Water. *J. Chem. Phys.* **1983**, *79* (2), 926–935.
- S4 Berendsen, H. J. C.; Postma, J. P. M.; van Gunsteren, W. F.; DiNola, A.; Haak, J. R. Molecular Dynamics with Coupling to an External Bath. *J. Chem. Phys.* **1984**, *81* (8), 3684–3690.
- S5 Nosé, S. A Unified Formulation of the Constant Temperature Molecular Dynamics Methods. *J. Chem. Phys.* **1984**, *81* (1), 511–519.
- S6 Abraham, M. J.; Murtola, T.; Schulz, R.; Páll, S.; Smith, J. C.; Hess, B.; Lindahl, E. GROMACS: High Performance Molecular Simulations through Multi-Level Parallelism from Laptops to Supercomputers. *SoftwareX* **2015**, *1–2*, 19–25.